

# Controlling the Growth Kinetics and Optoelectronic Properties of 2D/3D Lead–Tin Perovskite Heterojunctions


Edoardo Ruggeri, Miguel Anaya, Krzysztof Gałkowski, Géraud Delpont, Felix Utama Kosasih, Anna Abfalterer, Sebastian Mackowski, Caterina Ducati, and Samuel D. Stranks\*

Halide perovskites are emerging as valid alternatives to conventional photovoltaic active materials owing to their low cost and high device performances. This material family also shows exceptional tunability of properties by varying chemical components, crystal structure, and dimensionality, providing a unique set of building blocks for new structures. Here, highly stable self-assembled lead–tin perovskite heterostructures formed between low-bandgap 3D and higher-bandgap 2D components are demonstrated. A combination of surface-sensitive X-ray diffraction, spatially resolved photoluminescence, and electron microscopy measurements is used to reveal that microstructural heterojunctions form between high-bandgap 2D surface crystallites and lower-bandgap 3D domains. Furthermore, in situ X-ray diffraction measurements are used during film formation to show that an ammonium thiocyanate additive delays formation of the 3D component and thus provides a tunable lever to substantially increase the fraction of 2D surface crystallites. These novel heterostructures will find use in bottom cells for stable tandem photovoltaics with a surface 2D layer passivating the 3D material, or in energy-transfer devices requiring controlled energy flow from localized surface crystallites to the bulk.

In the past few years, hybrid metal halide perovskites with the  $ABX_3$  crystal structure have emerged as cost-effective materials showing great photovoltaic potential, with demonstrated lab-scale power conversion efficiency of 25.2%.<sup>[1–3]</sup> Furthermore, they provide cost-effective pathways for surpassing the Shockley–Queisser limit of single-junction technologies at the residential scale via perovskite/crystalline-Si or perovskite/perovskite tandem

configurations, with the current efficiency records standing at 28.0% and 25.0%, respectively.<sup>[1,4–7]</sup> One of the main benefits of perovskites is their versatility due to the tunability of their properties (notably, their bandgap  $E_g$ ) via compositional engineering of the A, B, and X species as well as via the introduction of large organic molecules that lead to the formation of low dimensional perovskite phases, among others.<sup>[6,8–14]</sup> The earliest metal-halide perovskites integrated into photovoltaics used only lead ( $Pb^{2+}$ ) at the B-site, delivering impressive performance and film quality.<sup>[15,16]</sup> Pb-based perovskites however possess bandgaps ( $E_g > 1.5$  eV) that are generally too high for optimal single-junction photovoltaic and other applications requiring light harvesting further into the near-infrared region. The bandgap can be lowered via B-site engineering through total or partial  $Pb^{2+}$  substitution with tin  $Sn^{2+}$ , with the lowest achievable bandgap of the mixed system to date reported to be  $\approx 1.2$ – $1.3$  eV. Sn-substitution brings the added benefit of reducing or removing toxic Pb.<sup>[17–28]</sup> The observed stability of the perovskite films is however reduced upon Sn-substitution as  $Sn^{2+}$  undergoes rapid oxidation to  $Sn^{4+}$ , disrupting the perovskite lattice, introducing a self-doping effect, and creating important carrier recombination centers that decrease the carrier diffusion length, lifetime, and the final device performance.<sup>[24,25,29–33]</sup> Solutions for this unwanted oxidation have been investigated, with

E. Ruggeri, Dr. M. Anaya, Dr. K. Gałkowski, Dr. G. Delpont, A. Abfalterer, Dr. S. D. Stranks  
Cavendish Laboratory  
University of Cambridge  
JJ Thomson Avenue, Cambridge CB3 0HE, UK  
E-mail: [sds65@cam.ac.uk](mailto:sds65@cam.ac.uk)

 The ORCID identification number(s) for the author(s) of this article can be found under <https://doi.org/10.1002/adma.201905247>.

© 2019 The Authors. Published by WILEY-VCH Verlag GmbH & Co. KGaA, Weinheim. This is an open access article under the terms of the Creative Commons Attribution License, which permits use, distribution and reproduction in any medium, provided the original work is properly cited.

DOI: 10.1002/adma.201905247

Dr. K. Gałkowski, Prof. S. Mackowski  
Institute of Physics  
Faculty of Physics  
Astronomy and Informatics  
Nicolaus Copernicus University  
5th Grudziadzka St., 87-100 Toruń, Poland

F. U. Kosasih, Prof. C. Ducati  
Department of Materials Science and Metallurgy  
University of Cambridge  
27 Charles Babbage Road, Cambridge CB3 0FS, UK  
Dr. S. D. Stranks  
Department of Chemical Engineering & Biotechnology  
University of Cambridge  
Philippa Fawcett Drive, Cambridge CB3 0AS, UK

the SnF<sub>2</sub> additive being the most commonly reported stability enhancer, but long-term solutions are not yet proven.<sup>[24,29–33]</sup>

2D low-dimensional Ruddlesden–Popper perovskite layers have been shown to be more stable than their 3D counterparts.<sup>[12,14,34–39]</sup> These are perovskite-like structures of the R<sub>2</sub>A<sub>n-1</sub>B<sub>n</sub>I<sub>3n+1</sub> form, where R is a large organic molecular cation spacer that forms planes periodically interrupting the 3D corner-sharing octahedra perovskite framework and protects the structure against oxygen and moisture penetration.<sup>[12,34–39]</sup> The physical confinement of the perovskite framework, however, leads to the formation of natural excitonic quantum wells, thus allowing one to modulate the bandgap of the material via the thickness of the well (*n*-number) and the bulkiness of the molecule R.<sup>[40–43]</sup> Most of the work on these 2D materials has been carried out on Pb-based compositions but only a handful of studies have been performed with Sn-based perovskites.<sup>[10,29,44–47]</sup> The hydrophobicity of the large cations could be particularly beneficial for the Sn and mixed-Pb:Sn systems as the 2D component could inhibit oxygen- and water-induced degradation pathways, bringing substantial improvements in ambient stability. Indeed, recent works demonstrated substantial improvements in mixed-Pb:Sn device operation and stability by employing 2D structures utilizing spacer molecules such as phenethylammonium (PEA)<sup>[48]</sup> and other analogues.<sup>[49,50]</sup> However, these device-focused studies do not allow one to ascertain information about the formation of the 2D component, how the fraction of 2D can be controlled and how the 2D component can influence carrier recombination and material stability.

Here, we show the integration of mixed-Pb:Sn perovskites into a highly stable self-assembled 2D/3D heterostructure architecture from a precursor solution of nominal PEA<sub>2</sub>FA<sub>2</sub>(Pb<sub>0.5</sub>Sn<sub>0.5</sub>)<sub>3</sub>I<sub>10</sub> (*n* = 3) composition, where FA is formamidinium. Hereafter, samples are identified by the nominal precursor solution composition. We demonstrate control over the relative fraction of 2D domains in the film via the introduction of an ammonium thiocyanate additive, and the influence of this additive on crystallization kinetics is probed via in situ X-ray diffraction (XRD) measurements during film formation. Finally, surface-sensitive

XRD and spatially and time-resolved photoluminescence, and electron microscopy measurements, reveal microstructural heterojunctions between high-gap 2D and low-gap 3D domains with distinctively unique optoelectronic properties. These tunable structures enhance our understanding of the growth and optoelectronic properties of 2D/3D perovskite heterojunctions, and will see use in energy funneling and passivating structures.

We processed a series of 2D/3D mixed perovskite films of the Pb:Sn family of nominal precursor solution composition PEA<sub>2</sub>FA<sub>2</sub>(Pb<sub>1-*y*</sub>Sn<sub>*y*</sub>)<sub>3</sub>I<sub>10</sub> (where *y* = 0–1 is the fractional B-site Sn content). **Figure 1a** shows the absorbance and photoluminescence (PL) spectra of the Pb:Sn series, with the higher energy PL regions amplified where stated for clarity. A top-view scanning electron microscopy (SEM) image of the *y* = 0.5 composition film is also shown in Figure 1b (see Figure S3 in the Supporting Information for other *y* compositions). The absorbance and PL data reveal two distinct regimes: a lower energy and a higher energy peak in each of the compositions. The lower energy features are attributed to bulk 3D Pb:Sn perovskites, while the higher energy peak shows exciton-like features (most prominent for the *y* = 0 composition) which we assign to 2D domains. The presence of these 2D domains is also confirmed by the low-angle peaks (i.e., *q* < 0.6 Å<sup>-1</sup>) in Grazing-Incidence Wide-Angle Scattering (GIWAXS) data (Figures S4 and S5, Supporting Information); we assign these low-angle peaks to reflections from 2D *n* = 1 and 2 domains.<sup>[40,45,51]</sup> These distinct 2D and 3D entities are also confirmed through local PL measurements (Figures S6 and S7, Supporting Information) that will be further discussed later. These results highlight the formation of distinct and segregated 2D and 3D domains each with its own absorbance and PL features.

We show the absorbance onset variation of both the higher and lower energy features in Figure 1b, revealing a bowing behavior for both the 2D and 3D domains, with minima for both domains at a Pb:Sn ratio of *y* = 0.75. The bowing behavior is a well-established phenomenon in 3D Pb:Sn perovskites,<sup>[19–23,26–28,52,53]</sup> but here we find that it also occurs in low-dimensional 2D domains. The origin of the bowing behavior

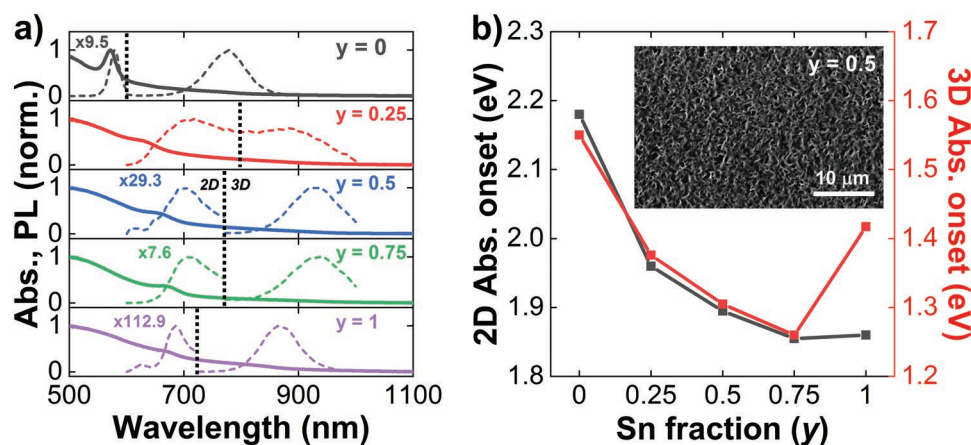


**Figure 1.** a) PL and absorbance spectra of the *y*-series of nominal precursor solution PEA<sub>2</sub>FA<sub>2</sub>(Pb<sub>1-*y*</sub>Sn<sub>*y*</sub>)<sub>3</sub>I<sub>10</sub>. PL spectra were acquired by excitation with a 405 nm laser with an excitation intensity of 10<sup>4</sup> mW cm<sup>-2</sup>. The PL spectra were separated into two regions, marked by the black vertical dotted lines, and the peak of highest intensity was normalized to 1. Where stated, the lower intensity peak was then multiplied by a factor (indicated) to be in turn normalized to 1. b) Absorbance onset values corresponding to the 2D (left axis) and 3D (right axis) domains as a function of Sn fraction (*y*) in the *y*-series of nominal precursor solution PEA<sub>2</sub>FA<sub>2</sub>(Pb<sub>1-*y*</sub>Sn<sub>*y*</sub>)<sub>3</sub>I<sub>10</sub>. The absorbance onsets were extracted from the spectra in Figure S1 in the Supporting Information through Tauc plots for the 3D domains (Figure S2, Supporting Information) and from the excitonic features for the 2D domains.

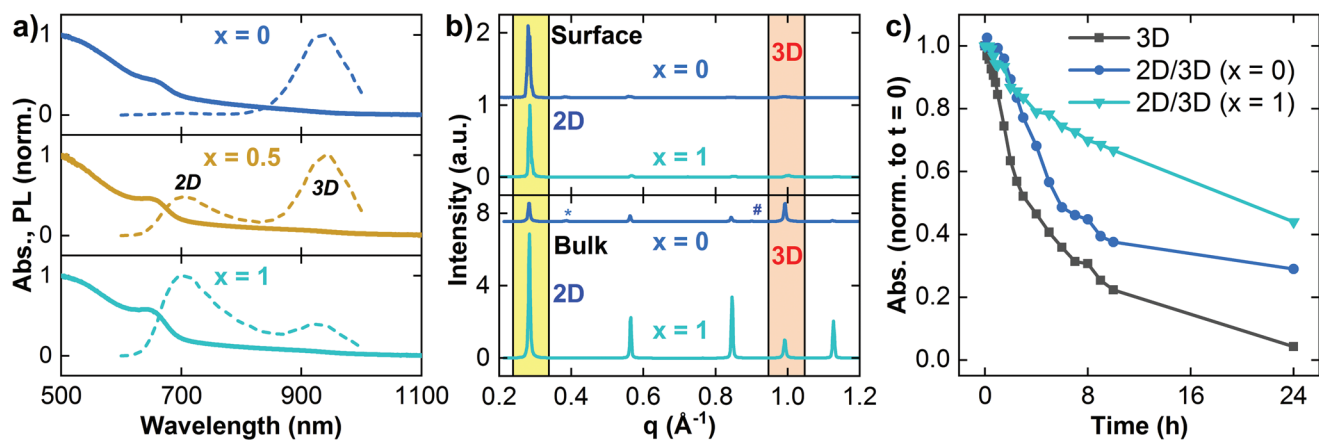


**Figure 2.** a) Normalized absorbance (solid curves) and PL (dotted curves) spectra of thin films from the nominal precursor solution  $\text{PEA}_2\text{FA}_2(\text{Pb}_{0.5}\text{Sn}_{0.5})_3\text{I}_{10}$  with increasing addition of AT additive ( $x$ ). PL spectra were acquired by excitation with a 405 nm laser with an excitation intensity of  $10^4 \text{ mW cm}^{-2}$ . b) Integrated GIWAXS (surface, top row) and bulk (XRD, bottom row) diffractograms of the nominal precursor solution  $\text{PEA}_2\text{FA}_2(\text{Pb}_{0.5}\text{Sn}_{0.5})_3\text{I}_{10}$  thin films with  $x = 0$  and  $x = 1$ . The yellow shaded area identifies the 2D  $n = 2$  peak (normalization center for GIWAXS data) and the brown shaded area identifies the 3D bulk peak (normalization center for XRD data). The \* and # symbols identify small fractions of 2D  $n = 1$  domains and  $\text{PbI}_2$ , respectively. c) Time-evolution of relative absorbance at 925 nm of the 2D/3D thin films from a nominal precursor solution of  $\text{PEA}_2\text{FA}_2(\text{Pb}_{0.5}\text{Sn}_{0.5})_3\text{I}_{10}$   $x = 0$  and  $x = 1$ , along with a 3D  $\text{FA}(\text{Pb}_{0.5}\text{Sn}_{0.5})\text{I}_3$  counterpart, over a period of 24 h in ambient laboratory conditions.

even in 3D perovskites is still debated. The most commonly reported origins include competition between spin–orbit coupling (reducing the bandgap) and lattice distortion (out-of-phase octahedral tilting in Pb-rich compositions increasing the bandgap),<sup>[28]</sup> and energy mismatch between Pb and Sn atomic orbitals forming the band edges of the perovskite alloy.<sup>[52]</sup> The observation of the bowing in low-dimensional domains adds support to the proposal of short-range effects, such as band edge mismatch or bond bending. Our collective results show that we form distinct 2D and 3D domains, though with a much greater fraction of 3D domains. We herein focus on the  $y = 0.5$  sample to further understand and control the 2D fraction and the resulting physical and optoelectronic properties.

In order to further tune the morphology and 2D/3D fractions, we introduced ammonium thiocyanate ( $\text{NH}_4\text{SCN}$ , hereafter shortened as AT) into the precursor solution, which has previously been shown to impact the orientation of 2D domains in Pb-only perovskite systems.<sup>[54,55]</sup> AT was added in different molar ratio concentrations into the precursor solution with respect to the PEA solution content, specifically no AT ( $x = 0$ ), 1:2 AT:PEA ( $x = 0.5$ ), and 1:1 AT:PEA ( $x = 1$ ), where we use  $x$  to denote the fraction of AT. **Figure 2a** shows the absorbance and PL data of the series with the AT additive. Strikingly, we observe that the addition of AT significantly increases the intensity of the high-energy 2D absorbance feature, as well as the high-energy PL peak (20-fold intensity increase for  $x = 1$  with respect to  $x = 0$ ), such that the high-energy feature becomes dominant for  $x = 1$ . We only observe a negligible variation in absorbance onset with addition of AT (Figures S8–S10, Supporting Information).

In **Figure 2b**, we show XRD and full-quadrant integrated GIWAXS (with low incidence angle of  $0.3^\circ$ ) data for the  $x = 0$  and  $x = 1$  compositions, allowing us to selectively probe the bulk (XRD) and surface (GIWAXS) structural properties (see Figures S11 and S12 in the Supporting Information for  $x = 0.5$  composition). In the GIWAXS data set, the  $q \approx 0.3 \text{ \AA}^{-1}$  peak corresponding to a 2D peak is normalized to 1, while in the XRD data set the  $q \approx 1 \text{ \AA}^{-1}$  peak corresponding to the 3D perovskite

domains is normalized to 1. For both samples, we see that this 2D peak is dominant on the surface through GIWAXS measurements, suggesting that the surfaces primarily consist of 2D domains in both cases. When we compare the bulk XRD for the samples, we find a substantially increased fractional intensity of the 2D peak with respect to the  $q = 1 \text{ \AA}^{-1}$  peak (3D domains) with increasing additive concentration ( $x$ ), consistent with a much larger fraction of 2D domains in the  $x = 1$  sample than  $x = 0$ . We note that the  $q = 1 \text{ \AA}^{-1}$  also increases in absolute intensity with  $x$  (Figure S13, Supporting Information). Determination of the  $d$ -spacing of the 2D XRD peak at  $q = 0.3 \text{ \AA}^{-1}$  reveals a crystallographic spacing distance of  $22.4 \text{ \AA}$ . This corresponds to  $n = 2$  domains when considering a perovskite octahedral contribution of  $\approx 6.5 \text{ \AA}$  and the contribution from  $\text{PEA}^+$  planes of  $\approx 10 \text{ \AA}$ .<sup>[40,45,51]</sup> The large organic spacer planes in this 2D/3D Pb:Sn configuration are found to be aligned parallel to the substrate (Figure S12, Supporting Information), unlike those reported in previous studies utilizing the same additive in Pb-only systems.<sup>[54,55]</sup> The introduction of AT also increases the  $n$ -number purity of the final film, as the peak at  $q = 0.4 \text{ \AA}^{-1}$  assigned to  $n = 1$  observed in the  $x = 0$  film (denoted as \* in **Figure 2b**), disappears in AT-containing compositions, yielding more phase-pure  $n = 2$  thin films. The traces of  $\text{PbI}_2$  also disappear in the AT-containing compositions. The combined absorbance, PL, diffraction and morphology results show a substantial increase in the relative fraction of 2D domains in the film with increasing  $x$ , with 2D domains prominently on the surface of the film.

To investigate the impact of the increased 2D fraction on perovskite stability, we tracked the evolution of the absorbance spectra of the  $x$ -series along with its bulk 3D thin film counterpart,  $\text{FA}(\text{Pb}_{0.5}\text{Sn}_{0.5})\text{I}_3$ . In order to assess the stability, we sampled the time-evolution of the absolute absorbance at 925 nm (3D domain absorbance onset) for unencapsulated samples in laboratory air conditions. We show in **Figure 2c** the absorbance evolution over a 24 h period, normalized relative to the value at  $t = 0$  (see Figure S14 in the Supporting Information for full absorbance spectra). We observe a significant increase

in ambient stability of the films with addition of the 2D component (PEAI); the 3D film retains only 30% of its initial absorbance in the 3D domains after the first 8 h, and only 5% after 24 h, while the 2D film ( $x = 0$ ) retains 45% and 30% of its initial absorbance after 8 and 24 h, respectively. Indeed, maximizing the presence of 2D material with AT boosts the stability of the AT-enriched films, with  $x = 1$  films retaining 70% of the initial absorbance after 8 h and 44% after 24 h. These results show that while 2D/3D thin films possess inherently higher oxygen and moisture stability with respect to their 3D counterparts, this can be further enhanced by increasing the relative fraction of 2D domains in the film via addition of AT.

We now seek to understand the film formation mechanism that leads to the enhanced fraction of 2D domains in these 2D/3D structures. To this end, we acquired in situ synchrotron GIWAXS measurements while annealing the films to form the desired perovskite compositions. The low incidence angle ( $0.3^\circ$ ) of the X-rays means the setup preferentially probes the nucleation and growth of 2D domains on the surface. This sensitive GIWAXS setup allows us to use low X-ray exposure dose to detect trace phases in the film that are not detectable with conventional laboratory XRD techniques, and also to continuously acquire a time series of diffraction snapshots due to short acquisition times.

For these in situ experiments, the precursor solution was first spin-coated onto a Si substrate in a nitrogen-filled glovebox

and transferred immediately ( $\approx 2$  min in a  $N_2$  filled passing tube) to the beamline in which they were annealed in inert conditions at  $100^\circ\text{C}$ . We show the in situ diffraction results during annealing for  $x = 0$  and  $x = 1$  in Figure 3a,d, respectively (see Figure S15 in the Supporting Information for overall formation results). We note that the broad scattering feature at early times ( $0$ – $120$  s) in the  $q = 0.4$ – $0.7 \text{ \AA}^{-1}$  range is due to a colloidal gel dispersion of perovskite precursors.<sup>[56–58]</sup> In order to track the nucleation and growth of the 2D and 3D domains, we studied the time-evolution of the full-quadrant  $q = 0.6 \text{ \AA}^{-1}$  (second order of the  $q = 0.3 \text{ \AA}^{-1}$  peak) and  $q = 1 \text{ \AA}^{-1}$  peaks, respectively. Integrated linecuts for these peaks are respectively reported in Figure 3b,c for  $x = 0$ , and Figure 3e,f for  $x = 1$ . We note that the final films formed on the beamline (Figure S16, Supporting Information) showed similar diffraction properties to those annealed ex situ in a nitrogen glove box (Figure S12, Supporting Information). In Figure 3a we observe that the nucleation of the 2D and 3D domains takes place simultaneously when no AT additive is employed, and that while 2D domains nucleate homogeneously, nucleation of the 3D domains starts with two separate peaks at  $q = 0.97 \text{ \AA}^{-1}$  and  $q = 0.99 \text{ \AA}^{-1}$  (see Figure 3b,c). As shown in Figure 3e,f, the growth of 2D domains in AT-enriched films show similar behavior to the films without the additive. However, strikingly, the addition of AT delays the nucleation of 3D domains with respect to the

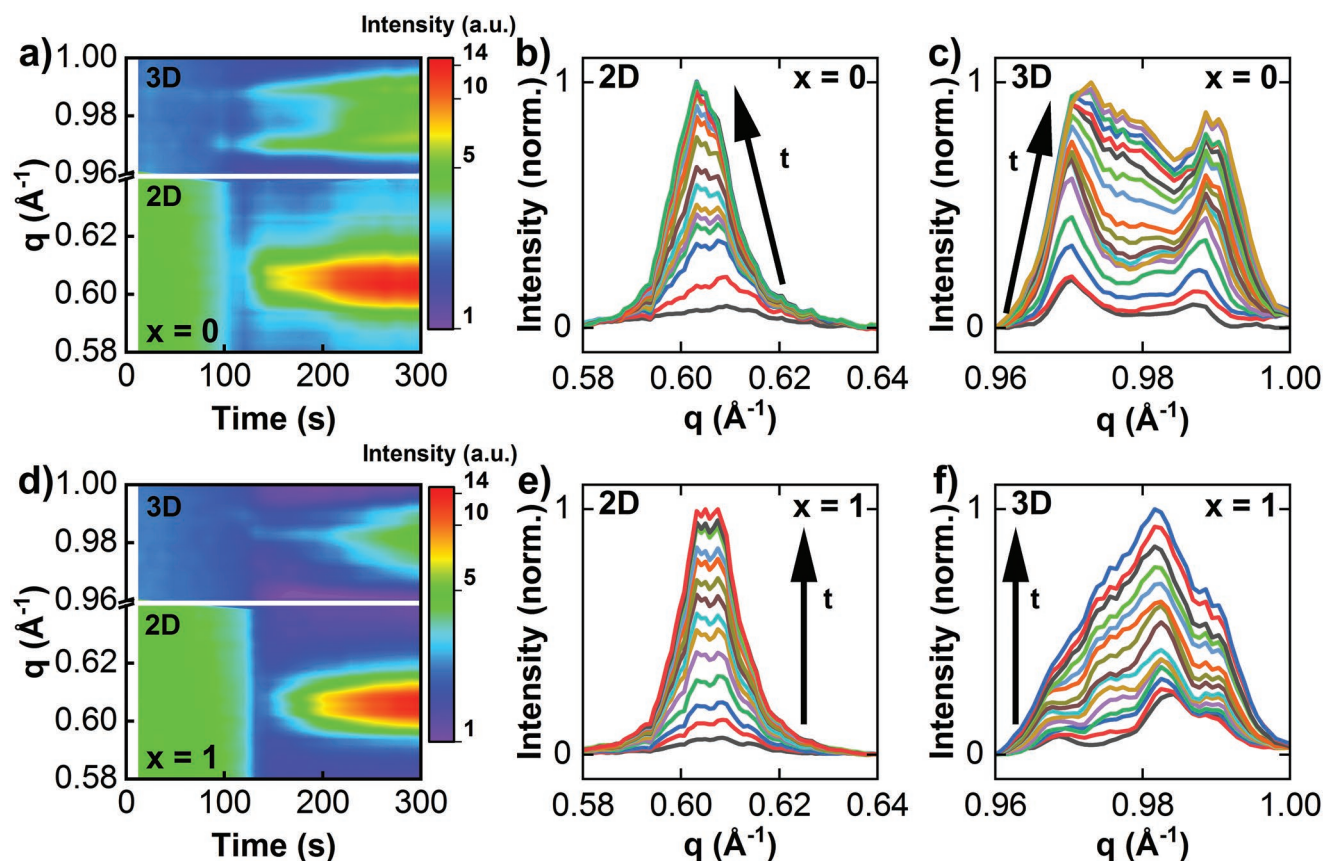


**Figure 3.** a,d) Quadrant-integrated GIWAXS intensity time-series plots tracking the growth of the 2D and 3D peak in the nominal precursor solution  $\text{PEA}_2\text{FA}_2(\text{Pb}_{0.5}\text{Sn}_{0.5})_{1-10}$  thin films without ( $x = 0$ ) (a) and with ( $x = 1$ ) (d) the AT additive. b,e) Integrated linecuts of the 2D peak in the  $x = 0$  (b) and  $x = 1$  (e) samples. c,f) Integrated linecuts of the 3D peak in the  $x = 0$  (c) and  $x = 1$  samples (f). Linecuts are taken at 12 s intervals starting at  $t = 120$  s in (a) and (b), and  $t = 144$  s in (d) and (f).

2D domains (Figure 3e), with an evident formation of a more homogeneous 3D peak (Figure 3f) than in the two-peak case without the additive (see data for  $x = 0.5$  sample in Figure S17 in the Supporting Information, which shows similar behavior to  $x = 1$ ). Furthermore, while the peaks in the  $x = 0$  sample shifted during nucleation and formation, the AT-containing samples exhibit more uniform peak growth. Therefore, the AT additive slows down the nucleation and crystallization of 3D domains, while also homogenizing the crystal structure. We propose that  $\text{NH}_4^+$  and  $\text{SCN}^-$  play the role of intermediaries, binding to the early colloids in the precursor solution suspension. This binding hinders the growth kinetics particularly of the 3D precursors, ultimately allowing nucleation only after evaporation of the  $\text{NH}_4\text{SCN}$  components during annealing. This proposition is consistent with reports of the  $\text{SCN}^-$  anion strongly interacting with  $\text{Pb}^{2+}$ <sup>[59,60]</sup> and the organic cations,<sup>[59,61]</sup> and the  $\text{NH}_4^+$  cation interacting with  $[\text{BI}_6]^{4-}$  ( $\text{B} = \text{Pb}, \text{Sn}$ ),<sup>[62,63]</sup> and then evaporating off during annealing (see the Supporting Information for further discussion).<sup>[17,54,55,61,64–66]</sup>

Now that we are able to selectively increase the 2D fraction in the perovskite films, we compare the optical and physical properties of the resulting structures by correlating morphological maps with spatially resolved luminescence properties on the same area. The same region of interest was tracked and identified in each experiment, with the help of unique fiducial scratches on

the film. We show these results for the  $x = 0$  (top row) and  $x = 1$  (bottom row) compositions in Figure 4 by comparing top-view SEM images (Figure 4a,e), and spatially resolved hyperspectral PL maps (Figure 4b,f) and PL lifetime maps (Figure 4c,g); see the same measurements for  $x = 0.5$  in Figure S18 and larger area maps in Figures S19–S21 in the Supporting Information. We show a schematic of the film structure and emission processes in Figure 4. The comparison between SEM images and hyperspectral maps reveals local needle and patch-like regions with areas on the surface showing high-energy emission ( $\approx 700$  nm) associated with 2D perovskite domains, and other regions showing lower energy emission domains ( $\approx 950$  nm) corresponding to 3D domains. Complementary atomic force microscopy (AFM; Figure S22, Supporting Information) and cross-sectional SEM (Figure S23, Supporting Information) images reveal that the 2D surface needle-like crystallites protrude 100–200 nm above the surface of the underlying  $\approx 200$ –300 nm 3D film, with a lateral dimension of 0.5–1  $\mu\text{m}$ . The local 2D emission can also be seen in the spatially resolved PL spectra in Figure 4d,h extracted from the locations marked on the hyperspectral maps (Figure 4b,f) with blue squares and the red triangles correspond to 3D-rich domains. The area-averaged PL spectra from the hyperspectral maps shown in Figure 4b,f also reveal that the relative area fraction of the high-energy peak increases with  $x$  (see also Figure S19 in the Supporting Information); the high-energy

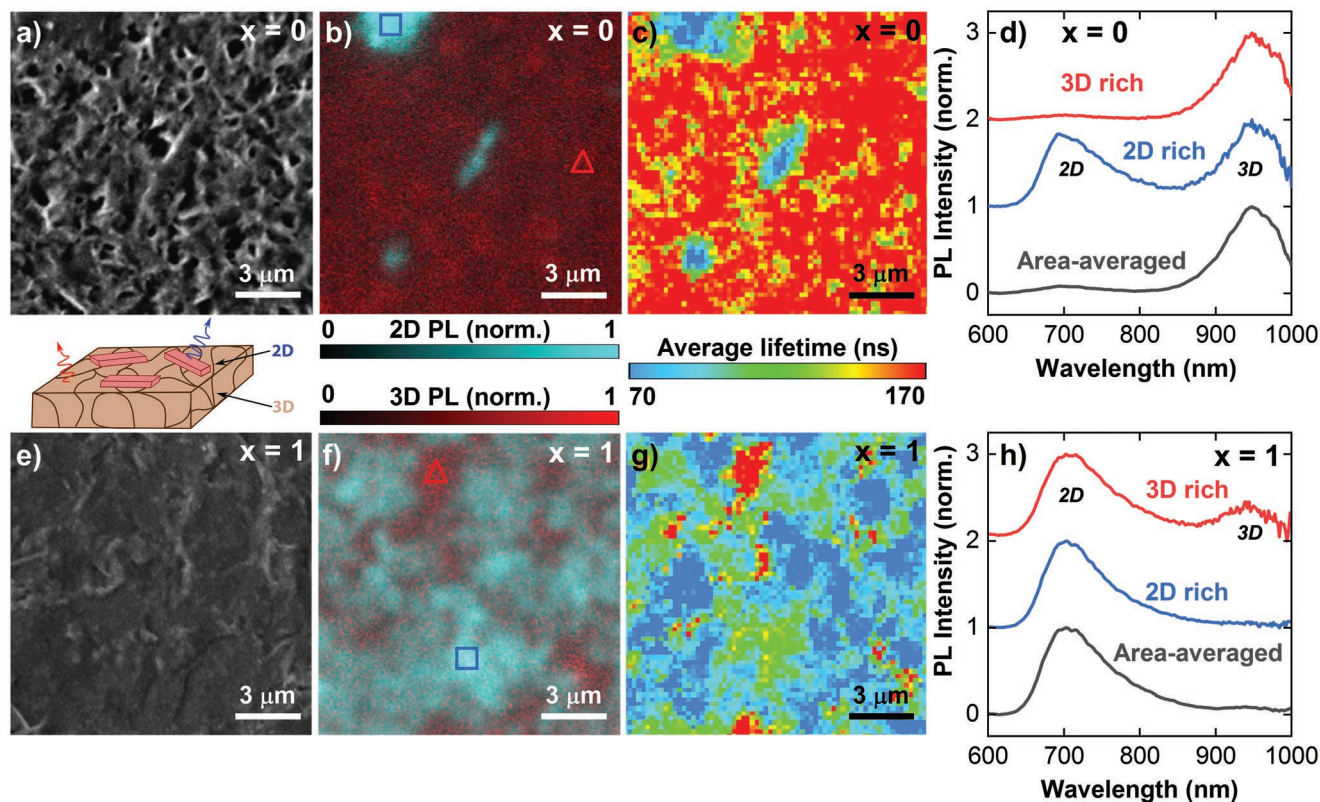


**Figure 4.** a–h) Top-view SEM images of thin films from the nominal precursor solution  $\text{PEA}_2\text{FA}_2(\text{Pb}_{0.5}\text{Sn}_{0.5})_3\text{I}_{10}$  without ( $x = 0$ ) (a) and with ( $x = 1$ ) (e) the AT additive, respectively correlated with spatially resolved hyperspectral PL (b,f) and confocal PL (c,g) lifetime maps. In between (a) and (e), we show a schematic of the morphology of the films and emission processes from the 2D and 3D domains. In the hyperspectral PL images, the blue squares and the red triangles respectively indicate the integrated areas for the local probing of the PL signal in 2D-rich and 3D-rich areas for the  $x = 0$  (d) and  $x = 1$  (h) samples. The hyperspectral false color maps are built by processing their hypercube according to an RGB color map, with the R channel centered at 950 nm and the B+G channels centered at 700 nm. Photoluminescence data were acquired with continuous wave (hyperspectral,  $10^4$   $\text{mW cm}^{-2}$ ) or pulsed (confocal, 2 MHz repetition rate, 1  $\mu\text{J cm}^{-2}$  per pulse) 405 nm lasers.

emission peak becomes dominant for the  $x = 1$  sample, consistent with a substantial increase in relative fraction of the 2D component in the film. Indeed, for the  $x = 1$  sample, an almost continuous surface-coverage crust of high-energy emitting 2D domains is observed, which is consistent with the SEM image in Figure 2c. The selective PL probing of 2D-rich (blue squares) and 3D-rich (red triangles) domains in  $x = 0$  shown in Figure 4d reveals that a strong low-energy emission signal is also present in 2D-rich probed regions, further indicating that these regions of surface 2D domains are preferentially located on top of a bed of 3D bulk material, consistent with our diffraction and morphological measurements. The 3D-rich regions also show a weak high-energy emission peak, indicating that some 2D domains may be dispersed amongst the 3D domains, either on the surface or buried deep within the bulk. We note that spatially-resolved chemical maps ascertained through energy-dispersive X-ray spectroscopy (EDX) maps on the same scan area do not show any local Pb:Sn composition differences between 2D and 3D domains, suggesting that they have similar Pb:Sn contents which are not further influenced by the additive (Figure S24, Supporting Information). Further correlation of these collective properties with average confocal PL lifetime maps (Figure 4c,g) shows that the 3D domains appear to have consistently longer average lifetimes with respect to the 2D domains, with 3D domains exhibiting PL lifetimes on the order of  $\approx 150$ – $200$  ns compared to  $\approx 30$ – $70$  ns for the 2D domains. The decreased lifetime in the 2D domains can be attributed to a combination of the excitonic nature of these 2D domains,<sup>[67–69]</sup> high local excitation densities on these localized crystallites, and competing energy transfer from 2D to 3D domains. These measurements further reinforce the high material and optoelectronic quality of these heterostructures.

Finally, the ability to tune the fraction of 2D and 3D components on the surface and the bulk opens up these heterostructures for a range of device applications. Recently, it was reported that the surface passivation of bulk lead-based 3D perovskite films with 2D molecules such as PEA through the post-treatment processing of PEA solutions can lead to extremely efficient and stable solar cells.<sup>[70–72]</sup> In that system, the large-bandgap 2D surface layer is sufficiently thin that charge injection to the contacts can still occur, though the layer still passivates trap states at the surfaces and grain boundaries of the 3D material. The self-assembled heterostructures presented in our work here could be optimized for application to low bandgap Pb:Sn 3D perovskite solar cells, relevant as bottom cells in tandem structures,<sup>[22,73]</sup> which to date are even more hindered by nonradiative losses and stability issues than their pure-lead counterparts.<sup>[7,74]</sup> In another example, the most efficient light-emitting diodes (LEDs) employing bulk perovskite films utilize 2D/3D mixed systems that allow an efficient cascade of injected carriers from the wider bandgap 2D materials to the lower bandgap 3D materials, leading to high luminescence efficiencies in the 3D layer.<sup>[51,75]</sup> Our photophysical measurements here demonstrate the signature of this energy cascade process in these heterostructures, which could be used for LEDs operating more stably and with emission deeper in the NIR than the typical lead-only systems.<sup>[9]</sup> The uncontrolled degree of formation of 2D and 3D domains has limited the use of both of these applications for Pb:Sn systems to date.<sup>[48–50]</sup> Such device applications will require tailored optimization of the heterostructures and will be the subject of future work.

In conclusion, we have fabricated 2D/3D solution-processed perovskite heterojunction films from  $\text{PEA}_2\text{FA}_2(\text{Pb}_{1-\gamma}\text{Sn}_\gamma)_3\text{I}_{10}$  ( $0 \leq \gamma \leq 1$ ) nominal precursor solutions. Surface and bulk diffraction measurements, combined with optical spectroscopy measurements, reveal that the 2D domains form preferentially on the surface of the films and stabilize the film properties. We find that an ammonium thiocyanate additive provides a lever to control the fraction of 2D and 3D domains in the films. In situ GIWAXS studies reveal that the additive delays the formation of the 3D domains, allowing growth of 2D domains to outcompete the 3D domain growth. By spatially correlating local morphology and photoluminescence measurements, we visualize the extensive surface coverage of the 2D domains and highlight the remarkably different optoelectronic properties of the 2D and 3D domains. Our findings emphasize the potential of compositional engineering to exploit the protective properties of 2D perovskites while simultaneously reducing the level of toxic Pb. These new heterostructures will be applicable to novel photovoltaic and thin film energy-transfer applications.

## Experimental Section

**Materials:** Phenethylammonium iodide (PEAI) and formamidinium iodide (FAI) were purchased from Greatcell Solar; ammonium thiocyanate ( $\text{NH}_4\text{SCN}$  —  $>98\%$ ), lead iodide ( $\text{PbI}_2$  —  $99.99\%$ ) and tin iodide ( $\text{SnI}_2$  —  $>97.0\%$ ) were purchased from TCI; tin fluoride ( $\text{SnF}_2$  —  $99\%$ ) was purchased from ACROS Organics; anisole (anhydrous,  $99.7\%$ ), dimethyl sulfoxide (DMSO — anhydrous,  $\geq 99.9\%$ ), and *N,N*-dimethylformamide (DMF — anhydrous,  $99.8\%$ ) were purchased from Sigma-Aldrich.

**Thin Film Fabrication:** 1 mm thick  $15 \times 15$  mm microscope glass slides were sequentially rinsed by 10 min sonication in acetone and 2-propanol, and dried via  $\text{N}_2$  gun blowing. The clean microscope slides were then treated in  $\text{O}_2$  plasma for 15 min. The pure-Pb solution was prepared by dissolving PEA (0.6 M), FAI (0.6 M), and  $\text{PbI}_2$  (0.9 M) in DMF (750  $\mu\text{L}$ ) and DMSO (250  $\mu\text{L}$ ) (3:1 volume ratio, v:v). The pure-Sn solution was prepared by dissolving PEA (0.6 M), FAI (0.6 M),  $\text{SnI}_2$  (0.9 M), and  $\text{SnF}_2$  (0.18 M) in DMF (750  $\mu\text{L}$ ) and DMSO (250  $\mu\text{L}$ ) (3:1 volume ratio, v:v). The mixed  $\text{PEA}_2\text{FA}_2(\text{Pb}_{1-\gamma}\text{Sn}_\gamma)_3\text{I}_{10}$  ( $0.25 \leq \gamma \leq 0.75$ ) were prepared by mixing the pure-Pb and pure-Sn solutions in separate vials according to  $\gamma$ , achieving  $\text{PbI}_2$  (( $1-\gamma$ )-0.9 M),  $\text{SnI}_2$  ( $\gamma$ -0.9 M), and  $\text{SnF}_2$  ( $\gamma$ -0.9)-0.02 M) in each solution. The solutions containing ammonium thiocyanate were prepared by weighing ammonium thiocyanate in separate vials and adding the volume of additive-free solution in order to achieve the desired ammonium thiocyanate concentration. The precursor solution (35  $\mu\text{L}$ ) was spin coated on a microscope slide at 4000 rpm for 30 s. Anisole antisolvent (200  $\mu\text{L}$ ) was dripped onto the substrate 20 s into the spin. The spin coated films were finally annealed at  $100^\circ\text{C}$  for 15 min. The thin films were then encapsulated by glue-assisted fixing of a 0.2 mm thick coverslip on the perovskite-side of the microscope slide. All solution preparation, spin coating, and encapsulation was carried out in an  $\text{N}_2$ -filled glovebox.

**Static and In Situ GIWAXS Measurements:** GIWAXS measurements were carried out at the I07 Surface and Interface Diffraction beamline at the Diamond Light Source in Didcot (United Kingdom). The beam energy was 10 keV (1.23985 Å). The scattered beam was collected by a Pilatus 2M large area detector, at a sample-detector distance of 0.4 m and calibrated with a silver behenate (AgBe) sample. The incidence angle was kept at  $0.3^\circ$  to achieve surface-preferential probing with a frame exposure of 1 s. The sample chamber was continuously purged with a  $1 \text{ L min}^{-1}$  He flow. For in situ measurements, substrates were spin coated in an adjacent  $\text{N}_2$ -filled glovebox for 2 s at 1000 rpm and then annealed at  $100^\circ\text{C}$  in the GIWAXS chamber.

**Atomic Force Microscopy Measurements:** Atomic force microscopy measurements were carried out in PeakForce tapping mode on a Bruker

Dimension Icon microscope with a Bruker ScanAsyst air tip, 45 kHz resonant frequency, 2 nm tip radius.

**Confocal Measurements:** Confocal time resolved photoluminescence images were measured using a confocal microscope setup (PicoQuant, MicroTime 200.) The excitation laser was a 405 nm pulsed diode (PDL 828-S“SEPIA II”, PicoQuant, pulsed width of around 100 ps) directly focused onto the perovskite surface with an air objective (100×, 0.9 NA). The laser intensity was  $1 \mu\text{J cm}^{-2} \text{ pulse}^{-1}$ . The photoluminescence signal was separated from the excitation light (405 nm) using a dichroic mirror (Z405RDC, Chroma). The photoluminescence was then focused onto a SPAD detector for the single photon counting (time resolution of 100 ps) through a pinhole (50  $\mu\text{m}$ ), with an additional 410 nm longpass filter. Repetition rates of 10 MHz were used for the maps. The raster scanning was performed using a galvo mirror system while both the objective and the sample remain at a fixed position. For the regular time-resolved PL map, both the excitation and the emission scanned through the mirror system.

**Hyperspectral PL Measurements:** Hyperspectral PL measurements were acquired using a wide-field IMA VISTM hyperspectral microscope from Photon Etc. equipped with a  $1040 \times 1392$  resolution silicon CCD camera, scanning the 600–1000 nm (500–1000 nm for  $\gamma = 0$ ) spectral range in 2 nm steps (1 nm for  $\gamma = 0$ ) with an exposure time of 5 s. The laser wavelength was 405 nm and its intensity  $10^4 \text{ mW cm}^{-2}$ . A 420 nm longpass filter was used before the detector to avoid damage. Overall PL spectra were acquired by integration of the hyperspectral map area. Area-specific spectra were acquired by integration of the correspondent area in the hyperspectral maps.

**Scanning Electron Microscopy/Energy-Dispersive X-ray Spectroscopy Measurements:** Top-view SEM images were acquired on a FEI Nova NanoSEM and a LEO GEMINI 1530VP FEG-SEM. An electron beam accelerated to 10 kV (Nova) and 5 kV (LEO GEMINI) was used. Cross-sectional SEM images were acquired on a Zeiss Crossbeam 540 with an acceleration voltage of 2 kV. All images were obtained in secondary electron mode with a through-the-lens Everhart–Thornley detector. EDX maps were acquired on a FEI Nova NanoSEM fitted with a Bruker XFlash 6 silicon drift detector with 100  $\text{mm}^2$  active area and processed in Esprit. EDX mapping was done with a 10 kV acceleration voltage, 790 pA beam current, and 4  $\mu\text{s pixel}^{-1} \text{ frame}^{-1}$  dwell time. Each final map is an average of 70–80 frames taken over a total mapping time of  $\approx 5$  min.

**UV–Vis Measurements:** UV–vis measurements were collected on an Agilent 8453 UV–vis spectrophotometer with deuterium (190–800 nm) and tungsten (310–1100 nm) lamps. It is equipped with a photodiode array for detection. UV–vis measurements for Tauc plots were collected on a Shimadzu UV-3600Plus spectrophotometer equipped with an integrating sphere for transmission measurements. It employs photomultiplier tube (165–870 nm), InGaAs (870–1650 nm), and PbS (1650–3300 nm) detectors and deuterium (165–282 nm) and tungsten (282–3300 nm) lamps. For transmission measurements, the samples were placed at the entrance of the integrating sphere. For stability measurements, the samples were kept in air in laboratory conditions and measured at predeterminate time intervals.

**X-Ray Diffraction:** XRD measurements were performed using a Bruker X-Ray D8 Advance diffractometer with  $\text{Cu K}\alpha_{1,2}$  radiation ( $\lambda = 1.541 \text{ \AA}$ ). Diffractograms were collected within an angular range of  $3^\circ \leq 2\theta \leq 40^\circ$  and with  $\Delta\theta = 0.01942^\circ$  steps.

## Supporting Information

Supporting Information is available from the Wiley Online Library or from the author.

## Acknowledgements

E. R., M.A., and S.D.S. acknowledge the European Research Council (ERC) under the European Union’s Horizon 2020 research and innovation program (HYPERION, grant agreement number 756962). E.R. was partially

supported by an EPSRC Departmental Graduate Studentship. S.D.S. acknowledges funding from the Royal Society and Tata Group (UF150033). M.A. acknowledges funding from the European Union’s Horizon 2020 research and innovation programme under the Marie Skłodowska-Curie (grant agreement number 841386). K.G. appreciates support from the Polish Ministry of Science and Higher Education within the Mobilnosc Plus program (Grant no. 1603/MOB/V/2017/0). G.D. would like to acknowledge the Royal Society for funding through a Newton International Fellowship. F.U.K. thanks the Jardine Foundation and Cambridge Trust for a doctoral scholarship. A.A. thanks the Royal Society for funding. This work utilized beamline I07 at the Diamond Light Source (Proposal S117223). The authors acknowledge the EPSRC (grant number EP/R023980/1).

## Conflict of Interest

The authors declare no conflict of interest.

## Keywords

heterojunction, low-dimensional, perovskites, photoluminescence, photovoltaics

Received: August 14, 2019

Revised: September 27, 2019

Published online:

- [1] NREL, “Best Research-Cell Efficiencies,” can be found under <https://www.nrel.gov/pv/assets/pdfs/best-research-cell-efficiencies.20191104.pdf> (accessed: November 2019).
- [2] A. E. Shalan, S. Kazim, S. Ahmad, *ChemSusChem* **2019**, *12*, 4116.
- [3] M. A. Green, E. D. Dunlop, D. H. Levi, J. Hohl-Ebinger, M. Yoshita, A. W. Y. Ho-Baillie, *Prog. Photovoltaics* **2019**, *27*, 565.
- [4] E. Köhnen, M. Jošt, A. B. Morales-Vilches, P. Tockhorn, A. Al-Ashouri, B. Macco, L. Kegelmann, L. Korte, B. Rech, R. Schlattmann, B. Stannowski, S. Albrecht, *Sustainable Energy Fuels* **2019**, *3*, 1995.
- [5] S. Rühle, *Phys. Status Solidi A* **2017**, *214*, 1600955.
- [6] W. Liao, D. Zhao, Y. Yu, N. Shrestha, K. Ghimire, C. R. Grice, C. Wang, Y. Xiao, A. J. Cimaroli, R. J. Ellingson, N. J. Podraza, K. Zhu, R.-G. Xiong, Y. Yan, *J. Am. Chem. Soc.* **2016**, *138*, 12360.
- [7] J. Tong, Z. Song, D. H. Kim, X. Chen, C. Chen, A. F. Palmstrom, P. F. Ndione, M. O. Reese, S. P. Dunfield, O. G. Reid, J. Liu, F. Zhang, S. P. Harvey, Z. Li, S. T. Christensen, G. Teeter, D. Zhao, M. M. Al-Jassim, M. F. A. M. Van Hest, M. C. Beard, S. E. Shaheen, J. J. Berry, Y. Yan, K. Zhu, *Science* **2019**, *364*, 475.
- [8] G. E. Eperon, S. D. Stranks, C. Menelaou, M. B. Johnston, L. M. Herz, H. J. Snaith, *Energy Environ. Sci.* **2014**, *7*, 982.
- [9] W. Qiu, Z. Xiao, K. Roh, N. K. Noel, A. Shapiro, P. Heremans, B. P. Rand, *Adv. Mater.* **2019**, *31*, 1806105.
- [10] L. Lanzetta, J. M. Marin-Beloqui, I. Sanchez-Molina, D. Ding, S. A. Haque, *ACS Energy Lett.* **2017**, *2*, 1662.
- [11] D. P. McMeekin, G. Sadoughi, W. Rehman, G. E. Eperon, M. Saliba, M. T. Hörantner, A. Haghighirad, N. Sakai, L. Korte, B. Rech, M. B. Johnston, L. M. Herz, H. J. Snaith, *Science* **2016**, *351*, 151.
- [12] D. H. Cao, C. C. Stoumpos, O. K. Farha, J. T. Hupp, M. G. Kanatzidis, *J. Am. Chem. Soc.* **2015**, *137*, 7843.
- [13] R. L. Milot, R. J. Sutton, G. E. Eperon, A. A. Haghighirad, J. Martinez Hardigree, L. Miranda, H. J. Snaith, M. B. Johnston, L. M. Herz, *Nano Lett.* **2016**, *16*, 7001.

- [14] C. C. Stoumpos, C. M. M. Soe, H. Tsai, W. Nie, J.-C. Blancon, D. H. Cao, F. Liu, B. Traoré, C. Katan, J. Even, A. D. Mohite, M. G. Kanatzidis, *Chem* **2017**, *2*, 427.
- [15] M. M. Lee, J. Teuscher, T. Miyasaka, T. N. Murakami, H. J. Snaith, *Science* **2012**, *338*, 643.
- [16] H.-S. Kim, C.-R. Lee, J.-H. Im, K.-B. Lee, T. Moehl, A. Marchioro, S.-J. Moon, R. Humphry-Baker, J.-H. Yum, J. E. Moser, M. Grätzel, N.-G. Park, *Sci. Rep.* **2012**, *2*, 591.
- [17] F. Gao, C. Li, L. Qin, L. Zhu, X. Huang, H. Liu, L. Liang, Y. Hou, Z. Lou, Y. Hu, F. Teng, *RSC Adv.* **2018**, *8*, 14025.
- [18] Q. Zhang, F. Hao, J. Li, Y. Zhou, Y. Wei, H. Lin, *Sci. Technol. Adv. Mater.* **2018**, *19*, 425.
- [19] E. S. Parrott, T. Green, R. L. Milot, M. B. Johnston, H. J. Snaith, L. M. Herz, *Adv. Funct. Mater.* **2018**, *28*, 1802803.
- [20] A. Rajagopal, R. J. Stoddard, H. W. Hillhouse, A. K.-Y. Jen, *J. Mater. Chem. A* **2019**, *7*, 16285.
- [21] R. Prasanna, A. Gold-Parker, T. Leijtens, B. Conings, A. Babayigit, H.-G. Boyen, M. F. Toney, M. D. McGehee, *J. Am. Chem. Soc.* **2017**, *139*, 11117.
- [22] G. E. Eperon, T. Leijtens, K. A. Bush, R. Prasanna, T. Green, J. T.-W. Wang, D. P. McMeekin, G. Volonakis, R. L. Milot, R. May, A. Palmstrom, D. J. Slotcavage, R. A. Belisle, J. B. Patel, E. S. Parrott, R. J. Sutton, W. Ma, F. Moghadam, B. Conings, A. Babayigit, H.-G. Boyen, S. Bent, F. Giustino, L. M. Herz, M. B. Johnston, M. D. McGehee, H. J. Snaith, *Science* **2016**, *354*, 861.
- [23] C. Wang, Z. Song, C. Li, D. Zhao, Y. Yan, *Adv. Funct. Mater.* **2019**, *29*, 1808801.
- [24] M. Konstantakou, T. Stergiopoulos, *J. Mater. Chem. A* **2017**, *5*, 11518.
- [25] N. K. Noel, S. D. Stranks, A. Abate, C. Wehrenfennig, S. Guarnera, A.-A. Haghighirad, A. Sadhanala, G. E. Eperon, S. K. Pathak, M. B. Johnston, A. Petrozza, L. M. Herz, H. J. Snaith, *Energy Environ. Sci.* **2014**, *7*, 3061.
- [26] M. Anaya, J. P. Correa-Baena, G. Lozano, M. Saliba, P. Anguita, B. Roose, A. Abate, U. Steiner, M. Grätzel, M. E. Calvo, A. Hagfeldt, H. Míguez, *J. Mater. Chem. A* **2016**, *4*, 11214.
- [27] Y. Zong, N. Wang, L. Zhang, M.-G. Ju, X. C. Zeng, X. W. Sun, Y. Zhou, N. P. Padture, *Angew. Chem., Int. Ed.* **2017**, *56*, 12658.
- [28] J. Im, C. C. Stoumpos, H. Jin, A. J. Freeman, M. G. Kanatzidis, *J. Phys. Chem. Lett.* **2015**, *6*, 3503.
- [29] S. Shao, J. Liu, G. Portale, H.-H. Fang, G. R. Blake, G. H. ten Brink, L. J. A. Koster, M. A. Loi, *Adv. Energy Mater.* **2018**, *8*, 1702019.
- [30] S. Gupta, D. Cahen, G. Hodes, *J. Phys. Chem. C* **2018**, *122*, 13926.
- [31] W. Liao, D. Zhao, Y. Yu, C. R. Grice, C. Wang, A. J. Cimaroli, P. Schulz, W. Meng, K. Zhu, R.-G. Xiong, Y. Yan, *Adv. Mater.* **2016**, *28*, 9333.
- [32] Z. Shi, J. Guo, Y. Chen, Q. Li, Y. Pan, H. Zhang, Y. Xia, W. Huang, *Adv. Mater.* **2017**, *29*, 1605005.
- [33] M. Xiao, S. Gu, P. Zhu, M. Tang, W. Zhu, R. Lin, C. Chen, W. Xu, T. Yu, J. Zhu, *Adv. Opt. Mater.* **2018**, *6*, 1700615.
- [34] I. C. Smith, E. T. Hoke, D. Solis-Ibarra, M. D. McGehee, H. I. Karunadasa, *Angew. Chem., Int. Ed.* **2014**, *53*, 11232.
- [35] H. Tsai, W. Nie, J.-C. Blancon, C. C. Stoumpos, R. Asadpour, B. Harutyunyan, A. J. Neukirch, R. Verduzco, J. J. Crochet, S. Tretiak, L. Pedesseau, J. Even, M. A. Alam, G. Gupta, J. Lou, P. M. Ajayan, M. J. Bedzyk, M. G. Kanatzidis, A. D. Mohite, *Nature* **2016**, *536*, 312.
- [36] T. M. Koh, V. Shanmugam, X. Guo, S. S. Lim, O. Filonik, E. M. Herzig, P. Müller-Buschbaum, V. Swamy, S. T. Chien, S. G. Mhaisalkar, N. Mathews, *J. Mater. Chem. A* **2018**, *6*, 2122.
- [37] R. Yang, R. Li, Y. Cao, Y. Wei, Y. Miao, W. L. Tan, X. Jiao, H. Chen, L. Zhang, Q. Chen, H. Zhang, W. Zou, Y. Wang, M. Yang, C. Yi, N. Wang, F. Gao, C. R. McNeill, T. Qin, J. Wang, W. Huang, *Adv. Mater.* **2018**, *30*, 1804771.
- [38] N. Li, Z. Zhu, C.-C. Chueh, H. Liu, B. Peng, A. Petrone, X. Li, L. Wang, A. K.-Y. Jen, *Adv. Energy Mater.* **2017**, *7*, 1601307.
- [39] F. U. Kosasih, C. Ducati, *ChemSusChem* **2018**, *11*, 4193.
- [40] B.-E. Cohen, M. Wierzbowska, L. Etgar, *Adv. Funct. Mater.* **2017**, *27*, 1604733.
- [41] X. Hong, T. Ishihara, A. V. Nurmikko, *Phys. Rev. B* **1992**, *45*, 6961.
- [42] Y. Chen, Y. Sun, J. Peng, J. Tang, K. Zheng, Z. Liang, *Adv. Mater.* **2018**, *30*, 1703487.
- [43] S. Silver, Q. Dai, H. Li, J.-L. Brédas, A. Kahn, *Adv. Energy Mater.* **2019**, *9*, 1901005.
- [44] D. B. Mitzi, C. A. Feild, W. T. A. Harrison, A. M. Guloy, *Nature* **1994**, *369*, 467.
- [45] Y. Liao, H. Liu, W. Zhou, D. Yang, Y. Shang, Z. Shi, B. Li, X. Jiang, L. Zhang, L. N. Quan, R. Quintero-Bermudez, B. R. Sutherland, Q. Mi, E. H. Sargent, Z. Ning, *J. Am. Chem. Soc.* **2017**, *139*, 6693.
- [46] P. Cheng, T. Wu, J. Liu, W.-Q. Deng, K. Han, *J. Phys. Chem. Lett.* **2018**, *9*, 2518.
- [47] L. Ma, M.-G. Ju, J. Dai, X. C. Zeng, *Nanoscale* **2018**, *10*, 11314.
- [48] J. Yuan, Y. Jiang, T. He, G. Shi, Z. Fan, M. Yuan, *Sci. China: Chem.* **2019**, *62*, 629.
- [49] D. Ramirez, K. Schutt, Z. Wang, A. J. Pearson, E. Ruggeri, H. J. Snaith, S. D. Stranks, F. Jaramillo, *ACS Energy Lett.* **2018**, *3*, 2246.
- [50] Z. Chen, M. Liu, Z. Li, T. Shi, Y. Yang, H.-L. Yip, Y. Cao, *iScience* **2018**, *9*, 337.
- [51] M. Yuan, L. N. Quan, R. Comin, G. Walters, R. Sabatini, O. Voznyy, S. Hoogland, Y. Zhao, E. M. Bearegard, P. Kanjanaboos, Z. Lu, D. H. Kim, E. H. Sargent, *Nat. Nanotechnol.* **2016**, *11*, 872.
- [52] A. Goyal, S. McKechnie, D. Pashov, W. Tumas, M. Van Schilfgaarde, V. Stevanović, *Chem. Mater.* **2018**, *30*, 3920.
- [53] A. Pisanu, A. Mahata, E. Mosconi, M. Patrini, P. Quadrelli, C. Milanese, F. De Angelis, L. Malavasi, *ACS Energy Lett.* **2018**, *3*, 1353.
- [54] X. Zhang, G. Wu, W. Fu, M. Qin, W. Yang, J. Yan, Z. Zhang, X. Lu, H. Chen, *Adv. Energy Mater.* **2018**, *8*, 1702498.
- [55] X. Zhang, G. Wu, S. Yang, W. Fu, Z. Zhang, C. Chen, W. Liu, J. Yan, W. Yang, H. Chen, *Small* **2017**, *13*, 1700611.
- [56] K. Yan, M. Long, T. Zhang, Z. Wei, H. Chen, S. Yang, J. Xu, *J. Am. Chem. Soc.* **2015**, *137*, 4460.
- [57] Y. Zhong, R. Munir, J. Li, M.-C. Tang, M. R. Niazi, D.-M. Smilgies, K. Zhao, A. Amassian, *ACS Energy Lett.* **2018**, *3*, 1078.
- [58] R. Munir, A. D. Sheikh, M. Abdelsamie, H. Hu, L. Yu, K. Zhao, T. Kim, O. El Tall, R. Li, D.-M. Smilgies, A. Amassian, *Adv. Mater.* **2017**, *29*, 1604113.
- [59] Q. Tai, P. You, H. Sang, Z. Liu, C. Hu, H. L. W. Chan, F. Yan, *Nat. Commun.* **2016**, *7*, 11105.
- [60] Q. Jiang, D. Rebolgar, J. Gong, E. L. Piacentino, C. Zheng, T. Xu, *Angew. Chem., Int. Ed.* **2015**, *54*, 7617.
- [61] H. Dong, Z. Wu, J. Xi, X. Xu, L. Zuo, T. Lei, X. Zhao, L. Zhang, X. Hou, A. K.-Y. Jen, *Adv. Funct. Mater.* **2018**, *28*, 1704836.
- [62] A. Sánchez-Coronilla, J. Navas, J. J. Gallardo, E. I. Martín, D. De Los Santos, N. C. Hernández, R. Alcántara, J. H. Toledo, C. Fernández-Lorenzo, *J. Nanomater.* **2017**, *2017*, 9768918.
- [63] Y. Rong, X. Hou, Y. Hu, A. Mei, L. Liu, P. Wang, H. Han, *Nat. Commun.* **2017**, *8*, 14555.
- [64] W. Ke, C. Xiao, C. Wang, B. Saparov, H.-S. Duan, D. Zhao, Z. Xiao, P. Schulz, S. P. Harvey, W. Liao, W. Meng, Y. Yu, A. J. Cimaroli, C.-S. Jiang, K. Zhu, M. Al-Jassim, G. Fang, D. B. Mitzi, Y. Yan, *Adv. Mater.* **2016**, *28*, 5214.
- [65] S. Yang, W. Liu, L. Zuo, X. Zhang, T. Ye, J. Chen, C.-Z. Li, G. Wu, H. Chen, *J. Mater. Chem. A* **2016**, *4*, 9430.
- [66] W. Fu, J. Wang, L. Zuo, K. Gao, F. Liu, D. S. Ginger, A. K.-Y. Jen, *ACS Energy Lett.* **2018**, *3*, 2086.
- [67] C. M. Mauck, W. A. Tisdale, *Trends Chem.* **2019**, *1*, 380.
- [68] C. Katan, N. Mercier, J. Even, *Chem. Rev.* **2019**, *119*, 3140.



- [69] G. Delport, G. Chehade, F. Lédée, H. Diab, C. Milesi-Brault, G. Trippé-Allard, J. Even, J.-S. Lauret, E. Deleporte, D. Garrot, *J. Phys. Chem. Lett.* **2019**, *10*, 5153.
- [70] J. J. Yoo, S. Wieghold, M. C. Sponseller, M. R. Chua, S. N. Bertram, N. T. P. Hartono, J. S. Tresback, E. C. Hansen, J.-P. Correa-Baena, V. Bulović, T. Buonassisi, S. S. Shin, M. G. Bawendi, *Energy Environ. Sci.* **2019**, *12*, 2192.
- [71] P. Chen, Y. Bai, S. Wang, M. Lyu, J.-H. Yun, L. Wang, *Adv. Funct. Mater.* **2018**, *28*, 1706923.
- [72] K. T. Cho, G. Grancini, Y. Lee, E. Oveisi, J. Ryu, O. Almora, M. Tschumi, P. A. Schouwink, G. Seo, S. Heo, J. Park, J. Jang, S. Paek, G. Garcia-Belmonte, M. K. Nazeeruddin, *Energy Environ. Sci.* **2018**, *11*, 952.
- [73] M. Anaya, G. Lozano, M. E. Calvo, H. Míguez, *Joule* **2017**, *1*, 769.
- [74] A. R. Bowman, M. T. Klug, T. A. S. Doherty, M. D. Farrar, S. P. Senanayak, B. Wenger, G. Divitini, E. P. Booker, Z. Andaji-Garmaroudi, S. Macpherson, E. Ruggeri, H. Sirringhaus, H. J. Snaith, S. D. Stranks, *ACS Energy Lett.* **2019**, *4*, 2301.
- [75] B. Zhao, S. Bai, V. Kim, R. Lamboll, R. Shivanna, F. Auras, J. M. Richter, L. Yang, L. Dai, M. Alsari, X.-J. She, L. Liang, J. Zhang, S. Lilliu, P. Gao, H. J. Snaith, J. Wang, N. C. Greenham, R. H. Friend, D. Di, *Nat. Photonics* **2018**, *12*, 783.